Excellent high cyclic fatigue properties of a novel ultrafine-grained medium entropy alloy

Shivakant Shukla[a,b,1], Rajiv S. Mishra[a,b*]

[a] Department of Materials Science and Engineering, University of North Texas, Denton, Texas 76207 USA

[b]Advance Materials and Manufacturing Processes Institute (AMMPI), University of North Texas, Denton, Texas, 76207 USA

**Corresponding author: Rajiv.Mishra@unt.edu*

[1]*Current Address: Oak Ridge National Laboratory, Oak Ridge, Tennessee 37830, USA*

Abstract

Fatigue is a major cause of failure and requires dedicated investigation to validate the integrity of potential structural materials. As high and medium entropy alloys (HEAs and MEAs) are garnering significant attention from scientific communities, it is important to test the structural integrity of these novel alloys in cyclic loading environment. This study analyzed both monotonic and cyclic loading properties of a novel medium entropy alloy (MEA) $CoCr_{1.3}Ni$ in the ultrafine-grained (UFG) and fine grain (FG) conditions. The UFG MEA performs better than the FG MEA during cyclic loading. Microstructural evolution after cyclic loading via electron back-scattered diffraction shows microstructural stability of both FG and UFG microstructures. Transmission electron microscopy suggests formation of stacking faults and fine-scale HCP transformation during cyclic loading.

Keywords: Medium entropy alloys; fatigue property; ultrafine-grained; Basquin equation analysis; stacking faults

1. Introduction

High entropy alloys (HEAs) have witnessed extensive attention in recent years from the worldwide scientific community. The exploration that commenced with single-phase FCC HEA of equiatomic composition (CoCrFeNiMn), also referred to as Cantor alloy [1], is ongoing, with various new compositional and novel multiphase HEAs being investigated. Despite all the advancements in multiphase HEAs, single-phase FCC HEAs continue to attract significant attention due to their good strength-ductility combination [2],[3], high irradiation resistance [4],[5], and cryogenic properties [6],[7].

Incipient literature on HEAs has assumed that increments in configurational entropy will lead to increases in solid solution strengthening [8],[9],[10]; thus, increasing the number of elements will improve the properties. However, support for this notion has been minimal. In the majority of the studies where excellent mechanical properties were reported, second-phase precipitates were also present in the matrix of HEAs [11], [12]. Hence, conclusive evidence that configurational entropy increments via additional elements will result in solid solution strengthening is still not fully convincing. Gali et al. [13] first demonstrated that by removing Mn from the Cantor alloy, slight improvement in mechanical properties of the single-phase FCC solid solution was achievable. In continuation, Gludovatz et al. [14] studied the damage tolerance behavior of the Cantor alloy and reported that by removing two elements (Fe and Mn), the resultant alloy had significantly better properties at cryogenic temperature. Reducing the number of alloying elements indeed reduces the configurational entropy; these ternary and quaternary compositions have been defined as medium entropy alloys (MEAs).

Lattice distortion, one of the four core effects of HEAs, originates from imperfect crystal lattice created via varying atomic radii of different principal elements. Mishra et al. [15] highlighted this

phenomenon by proposing that lattice distortion creates localized lattice strain, which impacts the mechanical properties. In addition, lattice distortion is responsible for variations in dislocation line energy due to fluctuations in lattice potential energy. During their investigation on MEA CoCrNi, Yoshida et al. [16] reported that local lattice distortion is also responsible for higher frictional stress when compared with the same of quinary CoCrFeNiMn HEA. Additionally, Tong et al. [17] studied evolution of local lattice distortion in CoCrFeNiMn HEA and its subsystem MEAs during irradiation and evaluated the elemental bond length via DFT calculation. Their study revealed that Cr-Cr bond distance showed maximum fluctuations when compared with other elemental bonds.

Fatigue is characterized as a damage accumulation process during service of a component. For materials to be applicable for structural applications, a foremost requirement is their fatigue strength. HEAs (or MEAs) are considered as potential substitutes for conventional alloys in structural as well as in other applications. Yet, the fatigue properties are rarely reported and hence their applicability is still hindered. Only a few studies have focused on the fatigue behavior of HEAs. Hemphill et al. [18] investigated the fatigue behavior of cold-rolled and annealed $Al_{0.5}$CoCrFeCuNi, with fatigue endurance falling between 540 and 945 MPa. Although they mistakenly reported the value of stress range rather than absolute value, their study revealed encouraging results in terms of microstructural evolution during fatigue. Shukla et al. [19] and Liu et al. [20] investigated fatigue properties of CoCrFeNi-based multiphase HEAs where multiscale features were attributed to delay in crack initiation, and the presence of nano-twins in the deformed region resulted in excellent fatigue properties. Moreover, Liu et al.'s [21],[22] investigations into the effect of transformation induced plasticity on fatigue properties suggested that metastability of the gamma phase has positive effects on fatigue properties.

In view of these studies, the current study investigates the fatigue property of a novel ultrafine-grained (UFG) MEA $CoCr_{1.3}Ni$ alloy. The given MEA system was selected based on the previous study [23], where systemically introduction of additional Cr atoms in the equiatomic CoCrNi MEA to increase the lattice distortion. Their study revealed that increased lattice distortion in $CoCr_{1.2}Ni$ and $CoCr_{1.3}Ni$ MEAs impacts both grain growth and mechanical property by reducing the former and increasing the later. Two different grain sizes were obtained (via cold-rolling and two different heat treatments) to understand the effect of grain size on cyclic loading properties. A detailed microstructural investigation before and after cyclic loading was performed.

2. Materials and method

2.1. Alloy preparation

The $CoCr_{1.3}Ni$ medium entropy alloy (MEA) was obtained from ACI Alloys, San Jose, California. The alloy was prepared via vacuum arc melting using high-purity (99.9%) individual elements. The MEA was flipped seven times to obtain homogeneity and was further homogenized in a vacuum atmosphere at 1200°C for 2 hours. After homogenization, cold-rolling to 70% of initial thickness was done on "IRM Model 5" x 8" hot lab rolling mills". Subsequent annealing at 700°C for 6 h and 800°C for 6 h was conducted on cold-rolled alloys. Two different heat treatments were performed to obtain different average grain sizes.

2.2. Microstructural characterization

To identify the phases present, X-ray diffraction (XRD) analysis was carried out using a Rigaku Ultima III diffractometer with Cu-Kα of wavelength 1.5718. The system was operated at a voltage of 40 kV and a current of 44 mA with a 2Θ range of 20°–90°. Basic microstructural analysis was done on FEI Nova NanoSEM 230 with field emission gun electron column. Orientation imaging microscopy (OIM) was performed on the same SEM system outfitted with TSL Digiview III electron backscattered diffraction (EBSD) detector. The step size for EBSD analysis was kept at 0.05 μm. Samples for both SEM and EBSD analysis were first polished to 1200 μm grit side paper and then 1 μm diamond polishing suspension on vel-cloth polishing cloth. Final polishing was done on the Beuehler VibroMet2 vibratory polisher using 0.02 μm colloidal silica liquid for 24 h to reduce any strain in the sample. Transmission electron microscopy analysis was done on the Tecnai G2 F20 S-Twin 200keV TEM operating at 200 kV. Samples for TEM were made via focused ion beam milling on an FEI Nova 200 NanoLab FIB/SEM dual-beam setup.

2.3. Tensile and fatigue property characterization

Tensile samples were made via a wire electric discharge machine (WEDM) with high dimensional accuracy. The dimensions of the mini-tensile specimen gage section are as follows: gage length of 5 mm, width of ~ 1.23 mm, and thickness of ~ 1.10 mm. Samples for tensile testing were polished to 1 μm surface finish. A custom-built computer-controlled testing system was employed to perform the mini-tensile tests. The tensile testing machine was equipped with a 500 lb load cell which is directly connected to one of the sample holding grips to measure the applied load. Additionally, a linear variable differential transformer (LVDT) measurement system was used to measure the displacement of the grips during the test.

Mini-fatigue testing of the samples was performed on a custom-built tabletop fully reversible (R=-1) bending mini fatigue testing machine. Dimensions and details regarding the fatigue testing machine can be found elsewhere [24]. Samples for fatigue testing were milled via mini-CNC machine and polished to surface finish of 0.02 μm to reduce any surface flaws. Microscopic analysis after fatigue testing was done on Nova NanoSEM 230. No subsequent polishing was done for EBSD post-failure. To preserve the fractured surface, minimal cleaning was performed for fractographic analysis.

3. Results

3.1. Initial microstructure characterization

After cold-rolling and annealing at two different temperatures, the initial microstructures were compared via electron backscattered diffraction (EBSD) and x-ray diffraction (XRD) analysis. Figure 1(a) presents an inverse pole figure (IPF) of $CoCr_{1.3}Ni$ alloy cold-rolled to 70% and heat-treated at 700°C for 6 h. Grain size distribution and misorientation angle plots are shown in Figures 1(b) and (c), respectively. Almost 75% have less than 1 μm grain size, and ~50% are smaller than 0.8 μm grain size. Additionally, a high fraction of twin boundaries, indicated by dark black color in Figure 1(a), can be noticed in misorientation plot (Figure 1 (c)). Since the average grain size of the given processing condition is 0.75 ± 0.35 μm, throughout this study, the 6 h heat-treated MEA will be referred to as UFG MEA. Figure 1(e) is an IPF of $CoCr_{1.3}Ni$ MEA cold-rolled to 70% of initial thickness and heat-treated at 800°C for 6 h. Clearly visible is an increase in grain size after heat-treatment at higher temperature; hence hereafter named fine-grain FG MEA. Figure 1(f) is a grain size distribution plot of FG MEA, while Figure 1(g) is the misorientation angle plot of the same. The average grain size is 1.4 ± 0.50 μm for FG condition, with 50% of the grain above 1 μm grain size. Although there is an increase of almost 100% in average grain size of FG MEA when compared with the same of UFG condition, the absolute increase is only ~0.60 μm. Similar trends were reported in the previous study by Komarasamy et al. [23], where the extra Cr restricted grain growth during annealing. Their study revealed that addition of extra Cr results in severe lattice distortion, consequently retarding the diffusion rates during annealing. Hence, a slow grain growth is expected which results in only a small increase in the average grain size of FG MEA. Furthermore, to confirm the phases present in both microstructures, XRD analysis of UFG and FG

MEA was conducted (Figure**s** 1(d) and (h), respectively). XRD plots reveal the peaks of only the FCC phase; hence, any presence of other major phases in both microstructures can be ruled out.

3.2. Tensile behavior analysis

We analyzed the mechanical response of both MEAs in quasi-static mode via mini-tensile tests. Figure 2(a) is a combined stress-strain plot of both microstructures (UFG and FG), where red and blue represent the tensile behavior of UFG and FG MEA, respectively. Engineering stress-strain curves are shown by solid lines, while dotted lines demonstrate true stress-strain curves. Figure 2(a) demonstrates that yield strength of UFG MEA is ~ 200 MPa higher than FG MEA. This can be attributed to the Hall-Petch phenomenon where decrease in the grain size positively affects the tensile properties. As the grain size of UFG MEA is-smaller than that of FG MEA, an increase of almost 200 MPa can be expected for–UFG MEA condition. In comparison, earlier studies on equiatomic CoCrNi MEA have put YS in the range of 550 MPa to 1100 MPa, for a grain size variation of 0.80 μm to 0.20 μm [16]. Similarly, Komarasamy et al. [23] have pointed out an increase in strength when Cr content is increased in equiatomic CoCrNi to $CoCr_{1.3}N$. The increase in strength can be attributed to increase in frictional stress due to addition of extra Cr in the present alloy. Both MEAs show a uniform elongation of ~15%. Figure 2(b) shows work-hardening rate (WHR) vs true strain curves for both alloys. In low SFE materials such as the current MEA, stage A of the work hardening curve (shown as the continuous drop) signifies dislocation slip-dominated plasticity domain. On the contrary, stage B (plateau type region) represents twinning/transformation-mediated plasticity regime of the work hardening [24],[25]. For a similar composition and two different grain size, stage B can shed light towards their twining ability during deformation. Investigation focusing on understanding the grain size effect on the extant of twinning and critical stress for twinning have demonstrated an inverse relationship between grain

size and fraction of twin as well as TWIP effect [26],[27]. Since UFG has lower grain size, we expect that hardening due to twinning maybe smaller than FG MEA. The WHR curves for both microstructures show a clear indication of twinning during deformation. Table 1 summarizes the findings of the aforementioned sections.

3.3. Fatigue property analysis

Fatigue property response in the high cycle regime was investigated via mini-fatigue testing in a fully reversible (R=-1) bending fatigue setup. Figure 3(a) demonstrates the S-N curve for both MEAs in the high cyclic fatigue region where the highest stress for testing was ~80 % of yield strength. In the stress amplitude ($\Delta\sigma/2$) vs number of cycles to failure (N_f) plot (Figure 3(a)), the UFG microstructure clearly demonstrates better fatigue life when compared with the FG MEA. Also, fatigue runout, the stress amplitude that corresponds to 10^7 number of cycles without failing, is higher for the UFG microstructure (~525 MPa) as compared to the FG (455 MPa). Since the quasi-static mechanical properties of both microstructures are different, another way of comparing fatigue properties is to normalize the load with UTS values of the specific material. Figure 3(b) demonstrates the normalized stress vs number of cycles to failure curve for UFG and FG MEA. Clearly visible is the better fatigue properties of UFG MEA at higher normalized stress. However, the curves for both microstructures merge at lower stress values, indicating a similarity in cyclic loading behavior at lower stress. It can also be interpreted that while at higher stresses the UFG microstructures performed better than the FG microstructure, the FG microstructure catches up to the UFG microstructure in a low-stress regime.

4. Discussion

4.1. Basquin eqation analysis

The mathematical analysis of fatigue life can be interpreted via the total strain fatigue life equation proposed by Landgraf [28] and Marrow [29]. Accordingly, total fatigue strain can be expressed in terms of plastic and elastic strain via the following equation:

$$\frac{\Delta\varepsilon_t}{2} = \frac{\Delta\varepsilon_{el}}{2} + \frac{\Delta\varepsilon_{pl}}{2} \tag{1}$$

where total strain, elastic strain, and plastic strain are represented by $\Delta\boldsymbol{\varepsilon}_t$, $\Delta\boldsymbol{\varepsilon}_{pl}$, and $\Delta\boldsymbol{\varepsilon}_{el}$, respectively. In the high cycle fatigue regime (HCF), plastic strain is much smaller than elastic strain ($\Delta\boldsymbol{\varepsilon}_{pl} << \Delta\boldsymbol{\varepsilon}_{el}$); while in low cycle fatigue (LCF) the plastic strain can be considered the dominant strain ($\Delta\boldsymbol{\varepsilon}_{pl} >> \Delta\boldsymbol{\varepsilon}_{el}$). Nevertheless, equation 1 can be rewritten in terms of strain as follows:

$$\frac{\Delta\varepsilon_t}{2} = \frac{\sigma'_f}{E}(2N_f)^b + \varepsilon'_f(2N_f)^c \tag{2}$$

where σ'_f and ϵ'_f are fatigue strength coefficient and fatigue ductility coefficient, while E is Young's modulus. Since in the current study tests were performed in HCF regime (Stress controlled), equation 2 can be modified to:

$$\frac{\Delta\varepsilon_t}{2} = \frac{\sigma'_f}{E}(2N_f)^b \tag{3}$$

$$\frac{E.\Delta\varepsilon_t}{2} = \frac{\Delta\sigma}{2} = \sigma'_f(2N_f)^b \tag{4}$$

Equation 4, known as Basquin relationship, relates stress amplitude to number of cycles (or precisely to the number of load reversals to failure). To better comprehend the mathematical relationship of the current MEA system, the S-N curve was fitted to the Basquin equation (equation 4), and the corresponding parameters were calculated and are plotted in Figure 4. Additionally,

datum points from the literature on high-strength Ti alloy [30], high-strength steel [31] and TWIP steel [32], all in the UFG regime, have been included for more objective analysis.

Figures 4(a) and (b) demonstrate fatigue strength coefficient (σ'_f) and fatigue strength (σ_{-1}) as functions of grain size. For the present study, both fatigue strength coefficient (σ'_f) and fatigue strength (σ_{-1}) increase as grain size decreases. Since generally tensile strength governs fatigue strength coefficient (σ'_f) and decreasing grain size increases tensile strength of the microstructure, an increase in both σ_f' *and* σ_{-1} is expected with decreasing grain size. Furthermore, for the corresponding grain size of 0.75 ± 0.35 μm, the UFG MEA shows the highest fatigue strength coefficient (σ'_f) when compared with UFG and TWIP steel. The higher value of (σ_f') comes from the inherent strengthening of UFG microstructure and extensive twinning during deformation. The fatigue strength exponent (b) is related to the damage mechanism in the microstructure and can shed light on the stability of the microstructure with respect to cyclic loading [33],[34],[35]. The value of *'b'* generally varies from -0.05 to -0.12 for most of the alloys. A smaller absolute value of *'b'* results in higher stability of the microstructures and hence can be associated with higher fatigue life if other Basquin equation parameters are kept constant. For the current UFG MEA, the absolute value of *'b'* is slightly higher than the FG microstructure and might be indicative of relative stability of the microstructure with respect to fatigue deformation (Figure 4(c)). Also, the twinning in FG MEA is more extensive than UFG MEA, a fact corroborated by the stage B of work hardening plot in Figure 2 (b) (for FG MEA blue color it is more sustained than UFG MEA red color). Since FG MEA has prolonged stage B work-hardening and bigger grain size, it is expected that the FG MEA will have a smaller value of 'b'. Additionally, TWIP steel demonstrating a very low value of fatigue strength exponent *'b'* indicates excellent microstructural stability, which might be due to the twinning induced plasticity around the crack tip helping to

dissipate the effect of stress. The combined effect of fatigue strength coefficient (σ'_f), fatigue strength (σ_{-1}) and fatigue strength exponent (b) can be visualized in the fatigue ratio (σ_{-1}/UTS) plot in Figure 4(d) which increases for the UFG microstructure as compared to the FG microstructure.

4.2. Microstructural evolution during cyclic loading

In conventional UFG alloys, grain coarsening is an observed microstructural phenomenon during fatigue testing. Grain coarsening occurs primarily due to dynamic recrystallization and indicates fatigue damage of the microstructure during testing [36]. Hence, microstructural analysis before and after fatigue testing was performed to understanding microstructural evolution during cyclic loading. To remove the impact of grain size on strength, samples for the post deformation study were fatigue-tested at ~0.55 of the UTS values. After fatigue failure, EBSD analysis close to the fractured region with same step size (0.05 μm) and same magnification provided a more quantifiable analysis. Figure 5(a), image quality (IQ) map, was obtained via orientational image microscopy (OIM) of the UFG MEA. The high angle grain boundaries (HAGBs) are shown in yellow, while on the same map coincidence site lattice (CSL) boundaries (Σ3, Σ9 and Σ27) are superimposed in blue color. Figure 5(d) is an OIM micrograph after fatigue failure of UFG MEA at location close to failure. The corresponding grain size and misorientation angle plots are shown in Figures 5 (b) and (c), respectively. The average grain size for UFG microstructure changes by a value of ~0.27 μm, and indicates minimum grain coarsening during cyclic loading. Moreover, the misorientation angle also seems to vary marginally after cyclic loading. Reduction in the fraction of Σ 3 boundaries (characterized by 60° misorientation) might be due to reduction or crack nucleation at twin boundaries [37],[38] although this needs to be clarified with higher resolution microscopy. Microstructural evolution for FG MEA is also analyzed via EBSD (Figure 5 (e–h). Figure 5(e) is an IQ map of the microstructure before fatigue; here again, yellow boundaries signify

the HAGBs, while blue boundaries imply the CSL boundaries. Similar color notation has been followed for the IQ map of fatigue failed samples (Figure 5(h)). The grain boundary and misorientation variations are presented in Figures 5(f) and (g), respectively. Grain size variation in the FG microstructure of ~0.15 μm is below the standard deviation values for the non-deformed sample. Similarly, scant variation in the misorientation angle plot confirms microstructure stability.

We also analyzed Kernel average misorientation (KAM) values for both microstructures before and after cyclic loading. KAM registers the misorientation between a point at the center of the Kernel and all points neighboring the kernel. KAM analysis quantifies the average misorientation around a measurement point, which can be used to understand local lattice distortion and strain energy within the microstructure. The misorientation values from zero to two degrees were examined and presented on a blue-to-red color scale, with blue denoting least and red denoting highest misorientation. Also, to keep the noise reduced, second nearest neighbors were selected for analysis. Figure*s* 6(a) and (b) correspond to the KAM map of UFG MEA before and after fatigue testing. Increases in KAM values of post-deformation samples clearly indicate high misorientation and hence can be related to accumulation of dislocation within the grains. This also ensures that the microstructure has less dislocation density prior to cyclic loading and hence could store dislocation during testing. Comparison between the non-deformed microstructures for both conditions also reveals that the FG microstructure has lower KAM values (Figure 6(c)) when compared with the UFG microstructure. Lower KAM values indicate a more capable microstructure in terms of dislocation storage, a fact that can be validated by the lower value of fatigue strength exponent (b) for FG MEA in Figure 4(c). The lower value of ‘b’ points towards higher stability of the microstructure and hence FG MEA with lower ‘b’ and lower KAM values

suggests better microstructural stability. Also, the overall increase in KAM values for FG MEA after fatigue failure in Figure 6(d) indicates storage of dislocations

Transmission electron microscopy (TEM) analysis after deformation was carried out to understand microstructural evolution after deformation in the UFG MEA. The FIB lift-out was carried out close to the failed region of the specimen, which failed after ~10^5 cycles at 750 MPa. The selected area electron diffraction (SAED) pattern of the fatigue failed samples (Figure 7(a)) indicates the presence of HCP lamellae in the FCC matrix. The corresponding bright-field TEM (BFTEM) image (Figure 7(b)) also reveals the presence of HCP lamellae in the FCC matrix. In medium-entropy CoCrNi alloys, Miao et al. [39] and Niu et al. [40] reported that small-scale transformation can occur on an atomic scale level along with the nano-twins and stacking faults. Hence, the $CoCr_{1.3}Ni$ can be considered a metastable alloy system. In metastable FCC alloys, the formation of HCP lamellae is expected around or close to the crack tip because of high stress. These transformations are responsible for the excellent fatigue properties in the given MEA. A well-recognized orientation relationship (OR) for FCC → HCP transformation, known as Shoji-Nishiyama OR, has also been established in the current study, where $< 1\bar{1}0 >_{FCC}$ is parallel to $< 11\bar{2}0 >_{HCP}$ [41],[42]. Further, high-resolution TEM (HRTEM) along $< 1\bar{1}0 >_{FCC}$ on the same fatigue failed sample was carried out. Figure 7(c), a HRTEM image of a specific location in Figure 6(b), thus indicates HCP region of ABAB stacking in the deformed FCC matrix. In addition, the weak beam dark field TEM analysis confirms the presence of stacking faults near the failed region (Figure 7(d)). Overall, FCC→ HCP transformation on a small-scale level, as well as stacking faults formation during fatigue testing, are responsible for the excellent fatigue strength exponent (b) and fatigue strength coefficient (σ'_f) derived in the previous section.

4.3. Fractographic analyis

In addition, fractographic analysis of the failed samples was performed to observe fatigue deformation features. Samples of both microstructural conditions were analyzed in secondary electron mode to differentiate various crack propagation stages. For more comprehensive fractographic analysis, stress values with respect to UTS were kept at ~0.55 for both conditions. Figure 8(a) is a macroscopic view of the fractured surface of UFG MEA tested at 650 MPa. Crack initiation points or nucleation points have been indicated via the arrow marks. The macroscopic view of the fractured surface can be divided into three distinct regions. Region I is generally a smooth region that includes crack initiation and stage I of crack propagation. Features such as river marks or beach marks as well as orientation of fatigue striation are important in identifying crack initiation points. In stage I, the crack generally propagates along the crystallographic direction; and hence in case of low SFE alloy, ridges and plateaus generally signify the planar slip motion responsible for plastic deformation during loading. Similar features have been observed in region I of FG alloys (Figure 8(d)). The magnified view of region II from UFG and FG MEAs is shown in Figures 8(b) and (e), respectively. Region II, which denotes stage II of crack propagation, is characterized by striation marking on the fracture surfaces. Fatigue striations are crack arrest markings and can be observed at low as well as high magnifications. According to Laird [43], fatigue striations are generally formed via plastic blunting and sharpening of the crack tip during cyclic deformation. A recent review article by Lynch [44] mentions that fatigue crack growth for intermediate ΔK_{th} values corresponds with macroscopic crack growth rate. Hence fatigue striation can be indicative of crack growth rate. Comparing striation spacing in both microstructures enables comparative analysis regarding stage II growth rate. Here, in Figure 8(b), striation spacing is bigger than in Figure 8(e); hence, the crack growth rate of UFG alloys is higher than that of the FG MEA. Additionally, the area covered by region II can also be proportional to time spent during stage II

of crack growth. Figures 8(a) and (d) reveal that in region I, crack initiation and stable crack growth rate occupy more area fraction in the UFG alloy as compared to the FG alloy. Thus, during fatigue life cycle, UFG MEA spends more time in crack initiation and stage I of crack propagation. Mughrabi et al. [36] and Mughrabi [45] have mentioned that resistance to crack initiation increases with decrease in grain size. Hence, a reasonable conclusion is that crack initiation time is higher in UFG microstructure when compared with FG MEA. Region III was the overload or final failure zone that occurred by void nucleation, coalescence, and growth, and consisted of a combination of coarse and fine dimples. The dimples on overload region indicates the ductile nature of the materials. Various studies have indicated that grain size has a positive relationship with the mean diameter of dimple [46],[47]. Given that the grain size of UFG MEA is smaller than the same of FG HEA, it can be expected that for the same stress ratio (0.55 of UTS), the average dimple diameter would be smaller.

5. Conclusions

To conclude, the $CoCr_{1.3}Ni$ medium entropy alloy (MEA) fabricated via casting and subsequent cold-rolling and annealing resulted in ultrafine-grained (UFG) and fine-grained (FG) microstructures. Both UFG and FG microstructures demonstrated excellent strength during monotonic deformation. The cyclic loading behavior of both microstructures showed excellent fatigue behavior, with UFG MEA performing better than FG MEA. Analysis based on the Basquin equation revealed that both fatigue strength coefficient and the exponent for MEA are higher than the same for conventional alloys. Orientation image microscopy analysis confirmed excellent microstructural stability, while transmission electron microscopy characterization exhibited the presence of stacking faults and HCP lamellae, which are responsible for excellent fatigue behavior.

6. Acknowledgment

Authors gratefully acknowledge the support of National Science Foundation (NSF) through grant no. 1435810. The assistance of Ms. Jessica Reeder at University of North Texas for fatigue sample preparation is also appreciated.

7. Data availability statement

The raw/processed data required to reproduce these findings cannot be shared at this time as the data also forms part of an ongoing study.

8. References

[1] B. Cantor, I.T.H. Chang, P. Knight, A.J.B. Vincent, Microstructural development in equiatomic multicomponent alloys, Materials Science and Engineering A. 375–377 (2004) 213–218. doi:10.1016/j.msea.2003.10.257.

[2] Z. Fu, B.E. MacDonald, Z. Li, Z. Jiang, W. Chen, Y. Zhou, E.J. Lavernia, Engineering heterostructured grains to enhance strength in a single-phase high-entropy alloy with maintained ductility, Materials Research Letters. 6 (2018) 634–640. doi:10.1080/21663831.2018.1526222.

[3] S.W. Wu, G. Wang, Y.D. Jia, J. Yi, Q.J. Zhai, C.T. Liu, B.A. Sun, H.J. Chu, J. Shen, P.K. Liaw, T.Y. Zhang, Enhancement of strength-ductility trade-off in a high-entropy alloy through a heterogeneous structure, Acta Materialia. 165 (2019) 444–458. doi:10.1016/j.actamat.2018.12.012.

[4] O. El-Atwani, N. Li, M. Li, A. Devaraj, J.K.S. Baldwin, M.M. Schneider, D. Sobieraj, J.S. Wróbel, D. Nguyen-Manh, S.A. Maloy, E. Martinez, Outstanding radiation resistance of tungsten-based high-entropy alloys, Science Advances. 5 (2019). doi:10.1126/sciadv.aav2002.

[5] N.A.P.K. Kumar, C. Li, K.J. Leonard, H. Bei, S.J. Zinkle, Microstructural stability and mechanical behavior of FeNiMnCr high entropy alloy under ion irradiation, Acta Materialia. 113 (2016) 230–244. doi:10.1016/j.actamat.2016.05.007.

[6] D. Li, C. Li, T. Feng, Y. Zhang, G. Sha, J.J. Lewandowski, P.K. Liaw, Y. Zhang, High-entropy Al 0.3 CoCrFeNi alloy fibers with high tensile strength and ductility at ambient and cryogenic temperatures, Acta Materialia. 123 (2017) 285–294. doi:10.1016/j.actamat.2016.10.038.

[7] Y. Tong, D. Chen, B. Han, J. Wang, R. Feng, T. Yang, C. Zhao, Y.L. Zhao, W. Guo, Y. Shimizu, C.T. Liu, P.K. Liaw, K. Inoue, Y. Nagai, A. Hu, J.J. Kai, Outstanding tensile properties of a precipitation-strengthened FeCoNiCrTi0.2 high-entropy alloy at room and cryogenic temperatures, Acta Materialia. 165 (2019) 228–240. doi:10.1016/j.actamat.2018.11.049.

[8] J.-W. Yeh, S.-K. Chen, S.-J. Lin, J.-Y. Gan, T.-S. Chin, T.-T. Shun, C.-H. Tsau, S.-Y. Chang, Nanostructured High-Entropy Alloys with Multiple Principal Elements: Novel Alloy Design Concepts and Outcomes, Advanced Engineering Materials. 6 (2004) 299–303. doi:10.1002/adem.200300567.

[9] D.B. Miracle, O.N. Senkov, A critical review of high entropy alloys and related concepts, Acta Materialia. (2017). doi:10.1016/j.actamat.2016.08.081.

[10] M.H. Tsai, J.W. Yeh, High-entropy alloys: A critical review, Materials Research Letters. 2 (2014) 107–123. doi:10.1080/21663831.2014.912690.

[11] S. Shukla, D. Choudhuri, T. Wang, K. Liu, R. Wheeler, S. Williams, B. Gwalani, R.S. Mishra, Hierarchical features infused heterogeneous grain structure for extraordinary strength-ductility synergy, (2018). doi:10.1080/21663831.2018.1538023.

[12] P. Shi, W. Ren, T. Zheng, Z. Ren, X. Hou, J. Peng, P. Hu, Y. Gao, Y. Zhong, P.K. Liaw, Enhanced strength–ductility synergy in ultrafine-grained eutectic high-entropy alloys by inheriting microstructural lamellae, Nature Communications. 10 (2019). doi:10.1038/s41467-019-08460-2.

[13] A. Gali, E.P. George, Tensile properties of high- and medium-entropy alloys, Intermetallics. 39 (2013) 74–78. doi:10.1016/j.intermet.2013.03.018.

[14] B. Gludovatz, A. Hohenwarter, D. Catoor, E.H. Chang, E.P. George, R.O. Ritchie, A fracture-resistant high-entropy alloy for cryogenic applications, Science. (2014). doi:10.1126/science.1254581.

[15] R.S. Mishra, N. Kumar, M. Komarasamy, Lattice strain framework for plastic deformation in complex concentrated alloys including high entropy alloys, Materials Science and Technology. 31 (2015) 1259–1263. doi:10.1179/1743284715Y.0000000050.

[16] S. Yoshida, T. Bhattacharjee, Y. Bai, N. Tsuji, Friction stress and Hall-Petch relationship in CoCrNi equi-atomic medium entropy alloy processed by severe plastic deformation and subsequent annealing, Scripta Materialia. 134 (2017) 33–36. doi:10.1016/j.scriptamat.2017.02.042.

[17] Y. Tong, G. Velisa, S. Zhao, W. Guo, T. Yang, K. Jin, C. Lu, H. Bei, J.Y.P. Ko, D.C. Pagan, Y. Zhang, L. Wang, F.X. Zhang, Evolution of local lattice distortion under irradiation in medium- and high-entropy alloys, Materialia. 2 (2018) 73–81. doi:10.1016/j.mtla.2018.06.008.

[18] M.A. Hemphill, T. Yuan, G.Y. Wang, J.W. Yeh, C.W. Tsai, A. Chuang, P.K. Liaw, Fatigue behavior of Al 0.5CoCrCuFeNi high entropy alloys, Acta Materialia. 60 (2012) 5723–5734. doi:10.1016/j.actamat.2012.06.046.

[19] S. Shukla, T. Wang, S. Cotton, R.S. Mishra, Hierarchical microstructure for improved fatigue properties in a eutectic high entropy alloy, Scripta Materialia. 156 (2018) 105–109. doi:10.1016/j.scriptamat.2018.07.022.

[20] K. Liu, M. Komarasamy, B. Gwalani, S. Shukla, R.S. Mishra, Fatigue behavior of ultrafine grained triplex Al0.3CoCrFeNi high entropy alloy, Scripta Materialia. 158 (2019) 116–120. doi:10.1016/j.scriptamat.2018.08.048.

[21] K. Liu, S.S. Nene, M. Frank, S. Sinha, R.S. Mishra, Metastability-assisted fatigue behavior in a friction stir processed dual-phase high entropy alloy, Materials Research Letters. 6 (2018) 613–619. doi:10.1080/21663831.2018.1523240.

[22] K. Liu, S.S. Nene, M. Frank, S. Sinha, R.S. Mishra, Extremely high fatigue resistance in an ultrafine grained high entropy alloy, Applied Materials Today. 15 (2019) 525–530. doi:10.1016/j.apmt.2019.04.001.

[23] M. Komarasamy, S. Shukla, N. Ley, K. Liu, K. Cho, B. McWilliams, R. Brennan, M.L. Young, R.S. Mishra, A novel method to enhance CSL fraction, tensile properties and work hardening in complex concentrated alloys — Lattice distortion effect, Materials Science and Engineering A. 736 (2018) 383–391. doi:10.1016/j.msea.2018.09.005.

[24] J. Shi, X. Sun, M. Wang, W. Hui, H. Dong, W. Cao, Enhanced work-hardening behavior

and mechanical properties in ultrafine-grained steels with large-fractioned metastable austenite, Scripta Materialia. 63 (2010) 815–818. doi:10.1016/j.scriptamat.2010.06.023.

[25] P.B. Hirsch, T.E. Mitchell, STAGE II WORK HARDENING IN CRYSTALS, Canadian Journal of Physics. 45 (1967) 663–706. doi:10.1139/p67-054.

[26] O. Bouaziz, S. Allain, C. Scott, Effect of grain and twin boundaries on the hardening mechanisms of twinning-induced plasticity steels, Scripta Materialia. 58 (2008) 484–487. doi:10.1016/j.scriptamat.2007.10.050.

[27] I. Gutierrez-Urrutia, S. Zaefferer, D. Raabe, The effect of grain size and grain orientation on deformation twinning in a Fe-22wt.% Mn-0.6wt.% C TWIP steel, Materials Science and Engineering A. 527 (2010) 3552–3560. doi:10.1016/j.msea.2010.02.041.

[28] R. Landgraf, The Resistance of Metals to Cyclic Deformation, in: Achievement of High Fatigue Resistance in Metals and Alloys, ASTM International, 2009: pp. 3-3–34. doi:10.1520/stp26837s.

[29] J. Morrow, Cyclic Plastic Strain Energy and Fatigue of Metals, in: Internal Friction, Damping, and Cyclic Plasticity, ASTM International, 2009: pp. 45-45–43. doi:10.1520/stp43764s.

[30] I.P. Semenova, A. V. Polyakov, G.I. Raab, T.C. Lowe, R.Z. Valiev, Enhanced fatigue properties of ultrafine-grained Ti rods processed by ECAP-Conform, in: Journal of Materials Science, 2012: pp. 7777–7781. doi:10.1007/s10853-012-6675-9.

[31] M.D. Chapetti, H. Miyata, T. Tagawa, T. Miyata, M. Fujioka, Fatigue strength of ultra-fine grained steels, Materials Science and Engineering A. 381 (2004) 331–336. doi:10.1016/j.msea.2004.04.055.

[32] A.S. Hamada, L.P. Karjalainen, A. Ferraiuolo, J. Gil Sevillano, F. De Las Cuevas, G. Pratolongo, M. Reis, Fatigue behavior of four high-Mn twinning induced plasticity effect steels, in: Metallurgical and Materials Transactions A: Physical Metallurgy and Materials Science, 2010: pp. 1102–1108. doi:10.1007/s11661-010-0193-7.

[33] R. Liu, Y. Tian, Z. Zhang, X. An, P. Zhang, Z. Zhang, Exceptional high fatigue strength in Cu-15at.%Al alloy with moderate grain size, Scientific Reports. 6 (2016). doi:10.1038/srep27433.

[34] F. Kun, H.A. Carmona, J.S. Andrade, H.J. Herrmann, Universality behind Basquin's law of fatigue, Physical Review Letters. 100 (2008). doi:10.1103/PhysRevLett.100.094301.

[35] S. Shukla, M. Komarasamy, R.S. Mishra, Grain size dependence of fatigue properties of friction stir processed ultrafine-grained Al-5024 alloy, International Journal of Fatigue. 109 (2018). doi:10.1016/j.ijfatigue.2017.12.007.

[36] H. Mughrabi, H.W. Höppel, Cyclic deformation and fatigue properties of very fine-grained metals and alloys, International Journal of Fatigue. 32 (2010) 1413–1427. doi:10.1016/j.ijfatigue.2009.10.007.

[37] Z.J. Zhang, P. Zhang, L.L. Li, Z.F. Zhang, Fatigue cracking at twin boundaries: Effects of crystallographic orientation and stacking fault energy, Acta Materialia. 60 (2012) 3113–

3127. doi:10.1016/j.actamat.2012.02.016.

[38] Z.F. Zhang, Z.G. Wang, Grain boundary effects on cyclic deformation and fatigue damage, Progress in Materials Science. 53 (2008) 1025–1099. doi:10.1016/j.pmatsci.2008.06.001.

[39] J. Miao, C.E. Slone, T.M. Smith, C. Niu, H. Bei, M. Ghazisaeidi, G.M. Pharr, M.J. Mills, The evolution of the deformation substructure in a Ni-Co-Cr equiatomic solid solution alloy, Acta Materialia. 132 (2017) 35–48. doi:10.1016/j.actamat.2017.04.033.

[40] C. Niu, C.R. LaRosa, J. Miao, M.J. Mills, M. Ghazisaeidi, Magnetically-driven phase transformation strengthening in high entropy alloys, Nature Communications. 9 (2018). doi:10.1038/s41467-018-03846-0.

[41] S. Matsumoto, A. Sato, T. Mori, Formation of h.c.p. and f.c.c. twins in an FeMnCrSiNi alloy, Acta Metallurgica Et Materialia. 42 (1994) 1207–1213. doi:10.1016/0956-7151(94)90137-6.

[42] W. Wu, L. Guo, B. Guo, Y. Liu, M. Song, Altered microstructural evolution and mechanical properties of CoCrFeNiMo0.15 high-entropy alloy by cryogenic rolling, Materials Science and Engineering A. 759 (2019) 574–582. doi:10.1016/j.msea.2019.05.078.

[43] The Influence of Metallurgical Structure on the Mechanisms of Fatigue Crack Propagation, in: Fatigue Crack Propagation, ASTM International, 2009: pp. 131-131–50. doi:10.1520/stp47230s.

[44] S. Lynch, S. Lynch, Some fractographic contributions to understanding fatigue crack growth, International Journal of Fatigue. 104 (2017) 12–26. doi:10.1016/j.ijfatigue.2017.06.036.

[45] H. Mughrabi, On the Grain-Size Dependence of Metal Fatigue: Outlook on the Fatigue of Ultrafine-Grained Metals, in: Investigations and Applications of Severe Plastic Deformation, Springer Netherlands, 2000: pp. 241–253. doi:10.1007/978-94-011-4062-1_31.

[46] W. Qin, J. Li, Y. Liu, J. Kang, L. Zhu, D. Shu, P. Peng, D. She, D. Meng, Y. Li, Effects of grain size on tensile property and fracture morphology of 316L stainless steel, Materials Letters. 254 (2019) 116–119. doi:10.1016/j.matlet.2019.07.058.

[47] M.H. Cai, C.Y. Lee, Y.K. Lee, Effect of grain size on tensile properties of fine-grained metastable β titanium alloys fabricated by stress-induced martensite and its reverse transformations, Scripta Materialia. 66 (2012) 606–609. doi:10.1016/j.scriptamat.2012.01.015.

Table 1. Grain size, Σ boundary fraction, yield strength, ultimate tensile strength and % elongation of UFG and FG $CoCr_{1.3}Ni$ medium entropy alloy

Material	Grain size (μm)	Σ boundary fraction (%)	Yield Strength (MPa)	Ultimate tensile strength (MPa)	% Elongation
FG MEA	1.4 ± 0.50	41	793 ± 7	1003 ± 10	15.5 ± 0.7
UFG MEA	0.75 ± 0.35	39	984 ± 6	1160 ± 9	14.3 ±1.07

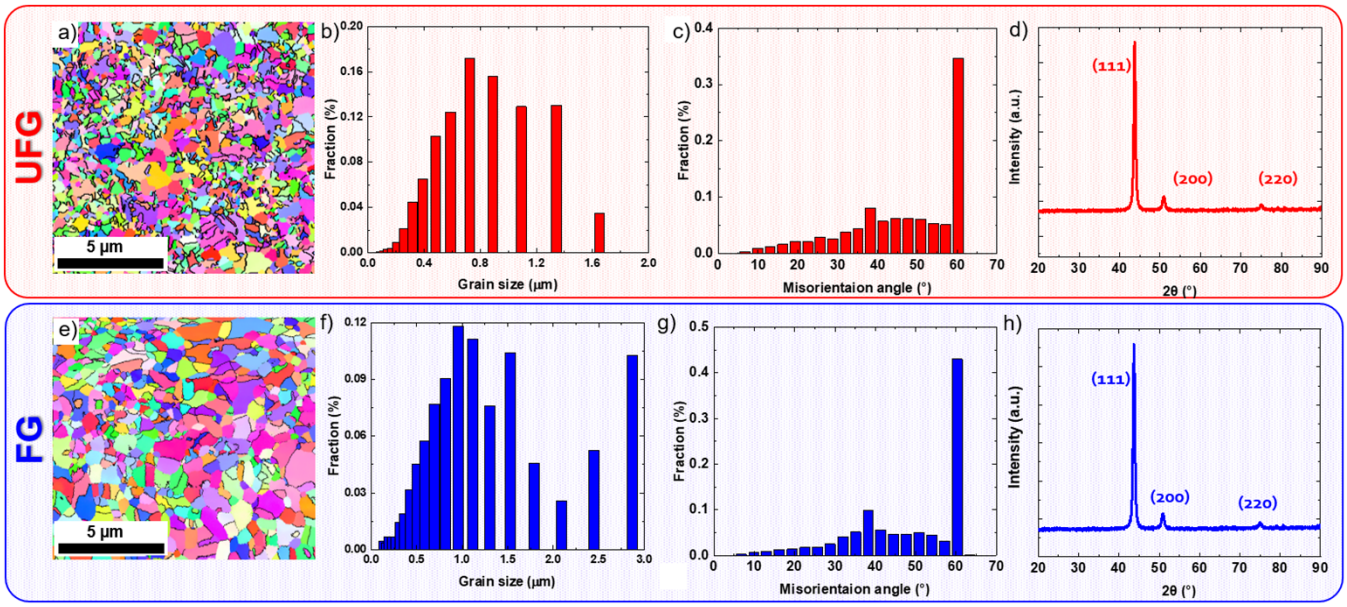

Figure 1. Microstructural characterization of 70% cold-rolled and heat-treated at 700°C for 6 h $CoCr_{1.3}Ni$ medium entropy alloy (MEA). (a) Inverse pole figure (IPF), (b) grain size distribution plot, (c) misorientation angle distribution plot and (d) x-ray diffraction (XRD) plot. This condition has been named (ultrafine-grained) UFG MEA due to the average grain size 0.75 ± 0.35 μm. (e) IPF, (f) grain size distribution plot, (g) misorientation angle distribution plot and (h) XRD plot of 70% cold-rolled and heat-treated at 800°C for 6 h $CoCr_{1.3}Ni$ medium entropy alloy (MEA), henceforth named (fine-grained) FG MEA due to average grain size of 1.4 ± 0.50 μm. Twin boundaries in both IPF maps have been indicated by dark black color.

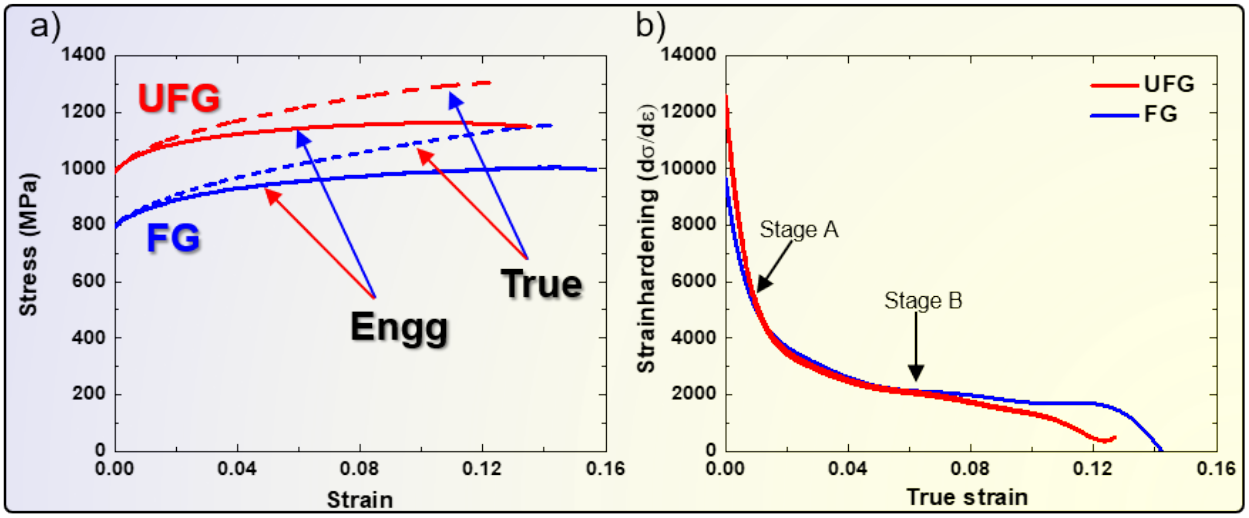

Figure 2. Mechanical property response of medium entropy alloy via (a) engineering and true stress strain curves. Red and blue colors represent the tensile behavior of UFG and FG MEA, respectively. Engineering stress-strain is shown in solid lines, while the dotted lines demonstrate the true stress-strain curves. (b) Strain hardening rate response with respect to true strain.

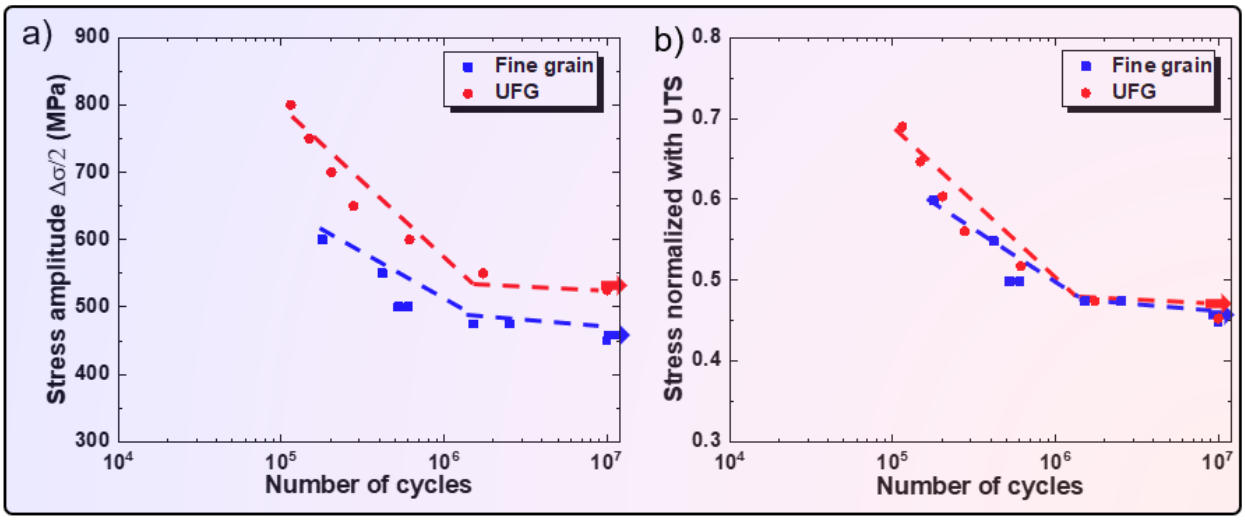

Figure 3. Cyclic property analysis of fine-grained and ultrafine-grained medium entropy alloys via (a) stress amplitude vs number of cycles to failure (S-N) curves and (b) UTS normalized stress vs number of cycles to failure curves.

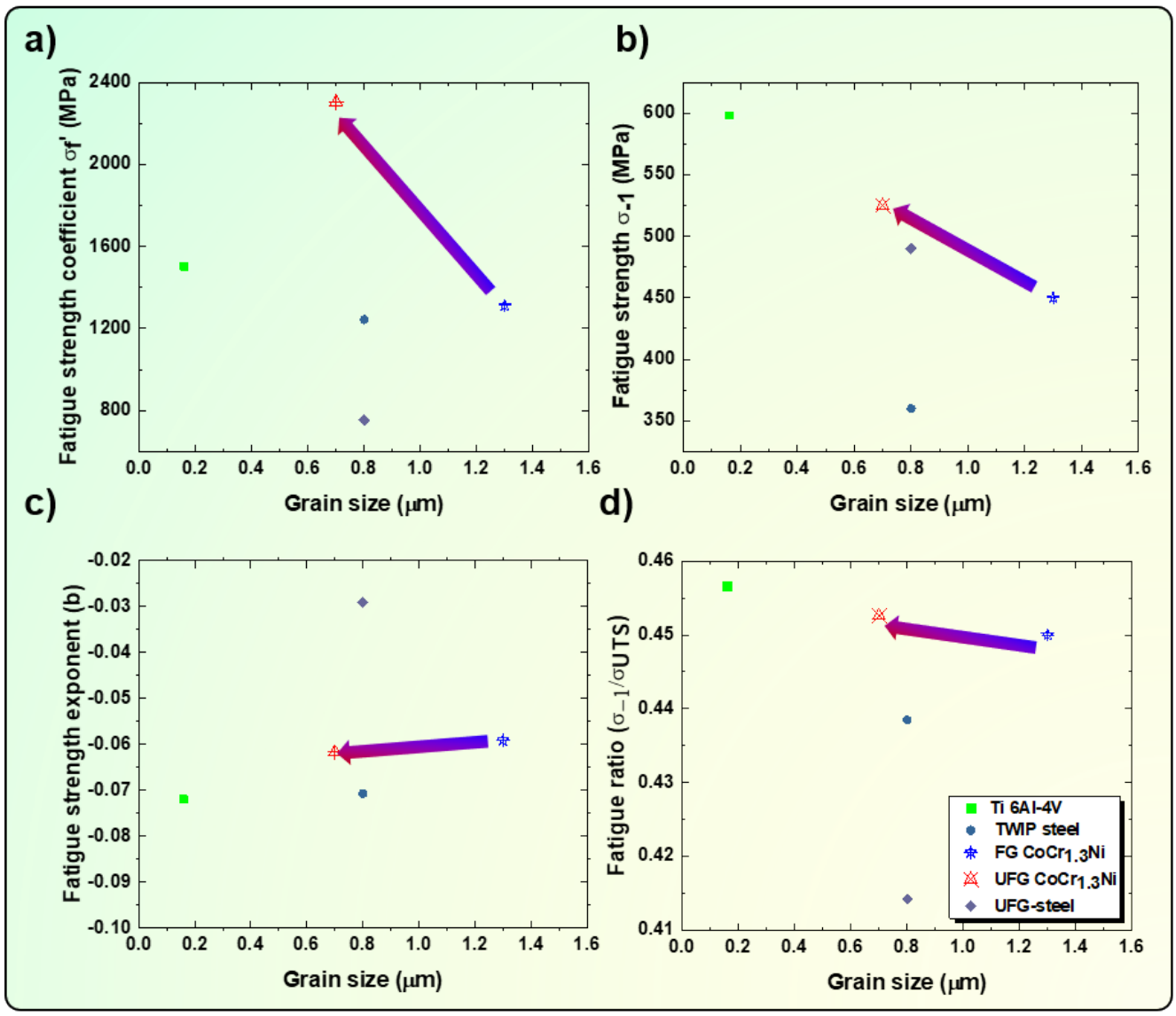

Figure 4. Basquin equation parameter analysis in terms of (a) fatigue strength coefficient (σ_f') vs grain size, (b) fatigue strength (σ_{-1}) vs grain size, (c) fatigue strength exponent (b) vs grain size and (d) fatigue ratio (σ_{-1}/UTS) vs grain size plots. σ_f' and *'b'* are parameters in the Basquin equation.

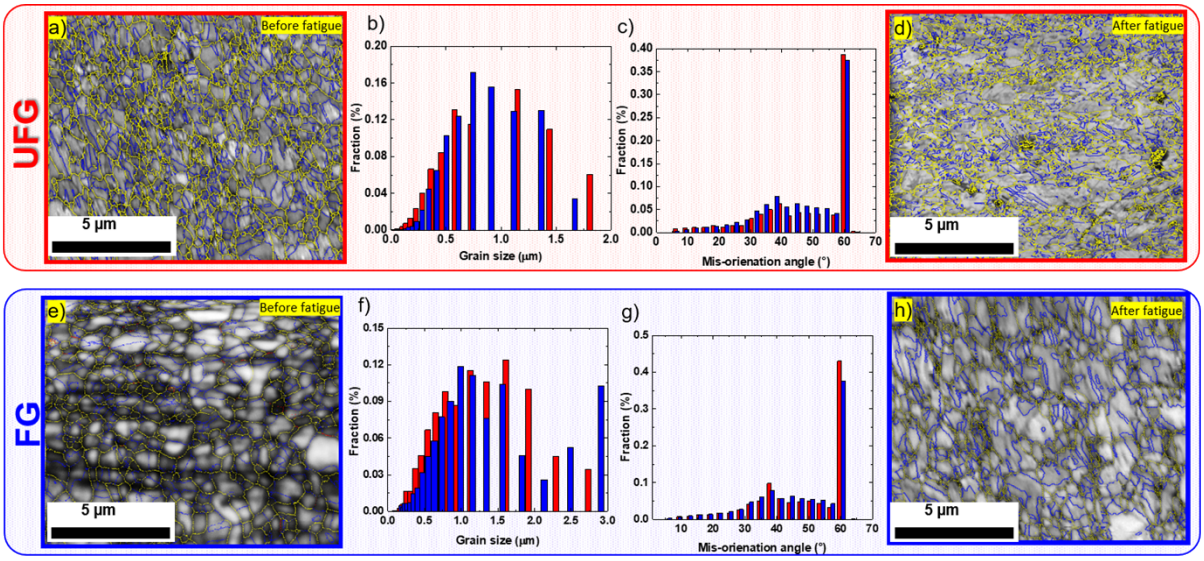

Figure 5. Image quality (IQ) map of UFG microstructure (a) before fatigue testing, (d) after fatigue testing and (b) and (c) corresponding grain size and misorientation angle variation plot. IQ map of FG microstructure (e) before fatigue testing, (h) after fatigue testing and (f) and (g) corresponding grain size and misorientation angle variation plots. Red and blue color data in plots b), c), f), and g) correspond to "before fatigue testing" and "after fatigue failure" respectively.

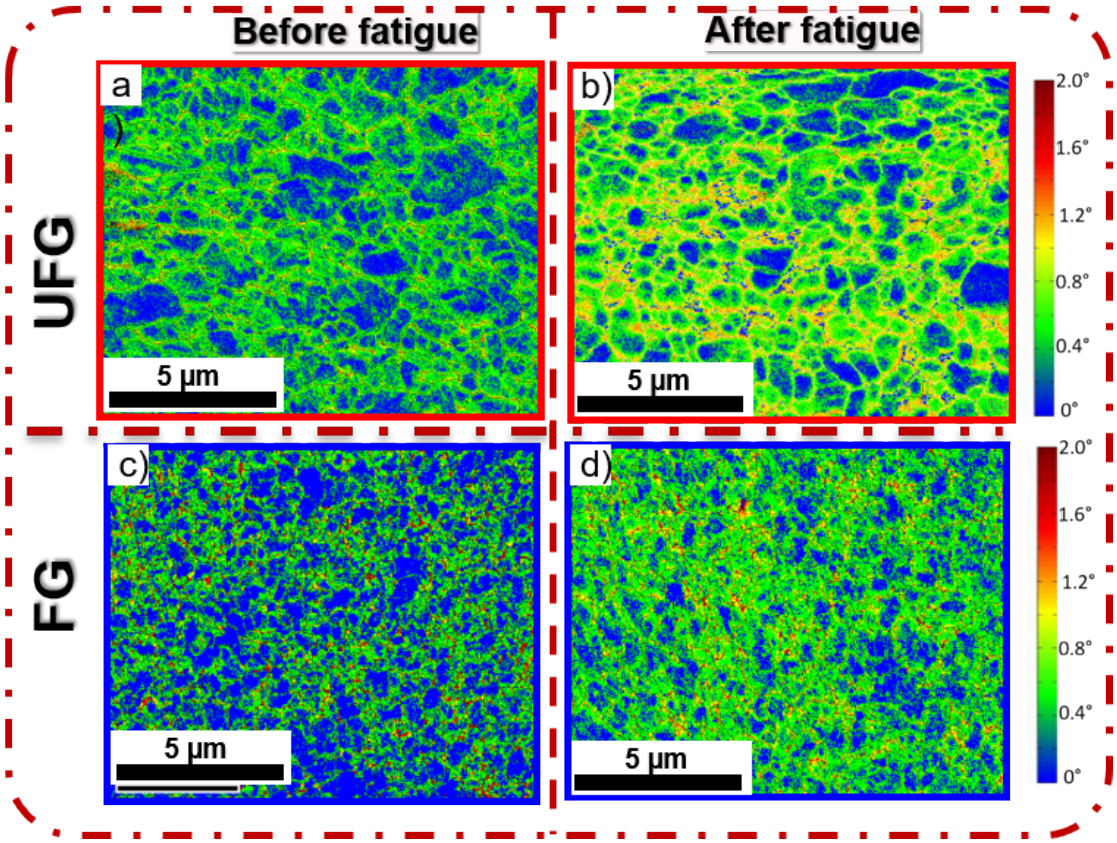

Figure 6. KAM variation maps for (a) before and (b) after fatigue tests for UFG microstructure. (c) and (d) KAM variation maps or FG microstructure before and after fatigue testing.

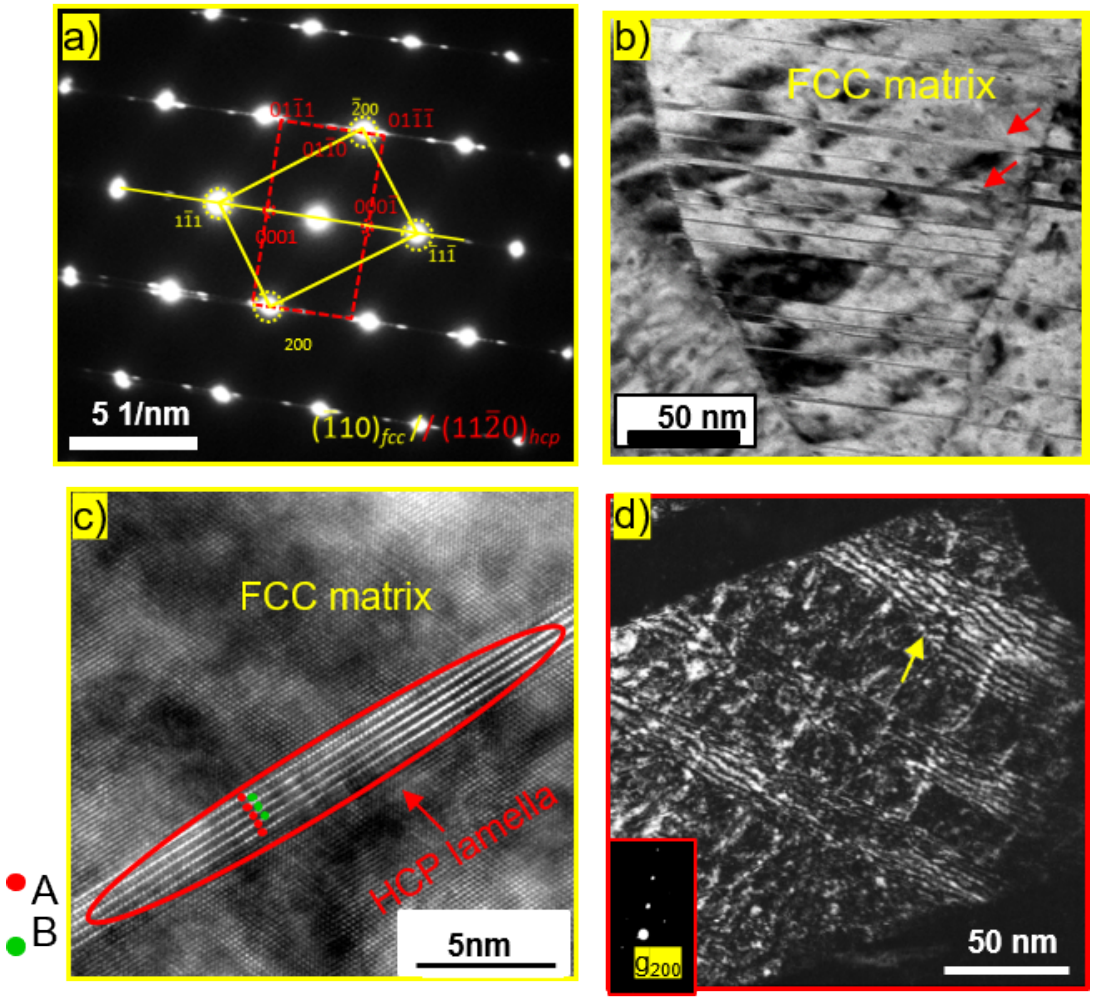

Figure 7. Transmission electron microscopy (TEM) analysis of ultrafine-grained $CoCr_{1.3}Ni$ post fatigue failure via (a) selected area diffraction pattern (SAED) demonstrating Shoji-Nishiyama orientation relationship between FCC and HCP and (b) corresponding bright field TEM (BFTEM) image showing HCP lamella (marked with red arrow) within the FCC matrix. (c) High resolution TEM (HRTEM) image of HCP lamella demonstrating ABAB stacking within the FCC matrix. (d) weak beam dark field (WBDF) image of the corresponding region showing stacking fault formation.

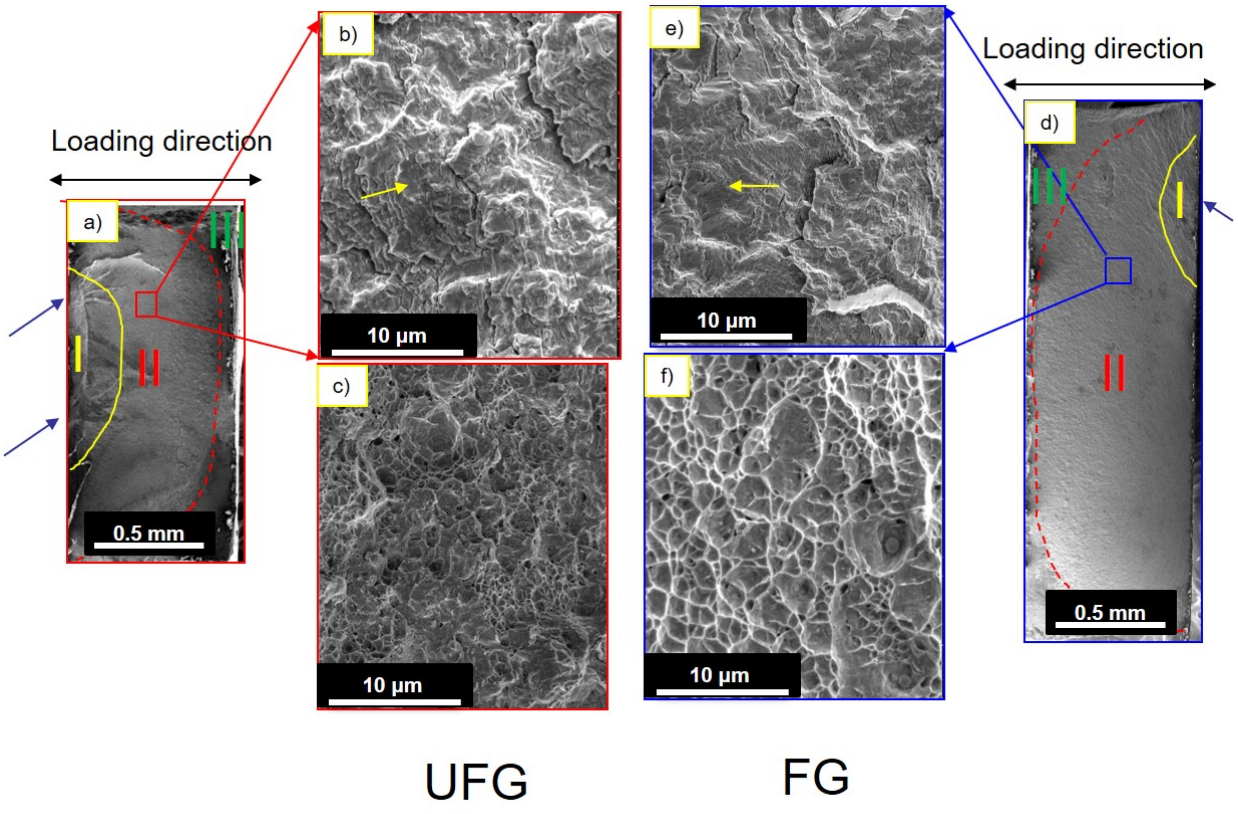

Figure 8. Fractographic images of failed UFG samples showing (a) macroscopic view, (b) region II and (c) region III. Fractographic images of failed FG samples showing (d) macroscopic view, (e) region II and (f) region III.